REVIEW PAPER

High-Frequency Surface-Wave Imaging from Traffic-Induced Noise by Selecting In-line Sources

Ling Ning[1] · Jianghai Xia[1] · Tianyu Dai[2] · Ya Liu[1] · Hao Zhang[1] · Chaoqiang Xi[3]

Abstract

Passive surface-wave methods have been given increased attention from the near-surface geophysics community because of their advantages of being low-cost and environment-friendly, especially in urban environments. The traffic noise sources, however, are not randomly distributed in time and space in densely populated urban areas. Stacking of cross-correlations is unable to effectively attenuate the azimuthal effects due to noise source distribution, resulting in overestimated surface-wave phase velocities. To solve this problem, we proposed a beamforming-based segment (i.e., time window) selection scheme that applies a beamforming technique with a pseudo-linear array to capture the noise segments coming from the sources in the stationary-phase zone. The azimuthal range of in-line noise sources is determined by the Fresnel angle calculated from the measured shortest wavelength. The cross-correlation is applied to these selected stationary-phase segments. The causal parts of cross-correlations are stacked to obtain the final virtual shot gather, since the single directional in-line noise sources are known through beamforming analysis. We used a synthetic test and two real-world examples of traffic-induced noise data acquired in urban environments to verify the feasibility of the proposed scheme. Results demonstrated that the proposed selection scheme can obtain virtual shot gathers with higher signal-to-noise ratio, higher-resolution dispersion energy, and accurate phase velocities, which provides an alternative tool for the applications of using passive surface-wave methods in urban environments, especially for the case of changes in distribution of noise sources in a short time.

Keywords Traffic-induced noise · Surface waves · Cross-correlation · Beamforming analysis · Segment selection

---

✉ Jianghai Xia
  jhxia@zju.edu.cn

1 Key Laboratory of Geoscience Big Data and Deep Resource of Zhejiang Province School of Earth Sciences, Zhejiang University, 38 Zheda Road, Hangzhou 310027, Zhejiang, China

2 School of Mathematics and Computer Sciences, Nanchang University, Nanchang 330031, Jiangxi, China

3 State Key Laboratory of Mining Response and Disaster Prevention and Control in Deep Coal Mines, School of Earth and Environment, Anhui University of Science and Technology, Huainan 232001, Anhui, China

Article Highlights

- The azimuthal range of in-line noise sources is defined by the first Fresnel angle calculated from the shortest wavelength
- A new segment selection scheme combines beamforming and cross-correlation to retrieve surface waves
- The proposed scheme produces higher-SNR virtual shot gathers and higher-resolution dispersion images

1 Introduction

The shear (S)-wave velocity as a function of depth is a key parameter for estimating the soil conditions in the shallow subsurface (Yilmaz et al. 2006). It can be derived by inverting phase velocities of surface waves (e.g., Dorman and Ewing 1962). Surface-wave methods play an extremely important role in estimating S-wave velocities, which are widely used for mapping bedrock interfaces (Miller et al. 1999; Xia et al. 2000), assessing the soil liquefaction potential (Lin et al. 2004; Devi et al. 2017), detecting subsurface anomalies (Mi et al. 2017, 2020), and investigating faults (Ivanov et al. 2006; Wu and Huang 2019). According to the origin of sources, surface-wave methods consist of active surface-wave methods and passive surface-wave methods, both of which ultimately produce near-surface S-wave velocity profiles to investigate the subsurface structures.

Hammers, accelerated weight drops, and harmonic shakers are commonly used as artificial, active sources. These sources can be utilized to generate strong high-frequency surface waves up to several tens of Hz. Owing to the advantages of being low-cost, environment-friendly, efficient, nondestructive, and noninvasive, the multichannel analysis of surface-waves (MASW) method (Song et al. 1989; Park et al. 1999; Xia et al. 1999) and the multichannel analysis of Love waves (MALW) method (Xia et al. 2012) perform very well in solving near-surface geological problems. They serve as powerful tools in estimating S-wave velocity by inverting surface-wave phase velocities. Surface waves, however, excited by the artificial sources are difficult to "see" deeper for the lack of lower (< 7 Hz) frequency data (Xia et al. 2003).

With the increasing demands on urban underground space investigation, new solutions are required to solve a variety of near-surface geological and geophysical problems. As passive surface waves, such as ocean-generated waves (< 0.2 Hz) and cultural noise ($>$ 1 Hz), are typically of a low-frequency nature, the passive surface-wave measurements provide a wide range of penetration depths (from a few tens of meters to a few kilometers) to solve numerous engineering problems. In recent years, passive surface-wave methods have rapidly aroused many researchers' keen interest (e.g., Zhang et al. 2019; Cheng et al. 2021b; Dai et al. 2021; Mi et al. 2022; Zhou et al. 2021, 2022), which provide the feasibility of producing near-surface S-wave velocities without artificial sources. These methods turn the "useless" noise into effective signals (e.g., surface waves), such as the spatial autocorrelation (SPAC) (Aki 1957; Luo et al. 2016), the refraction microtremor (ReMi) (Louie 2001; Stephenson et al. 2005), the seismic interferometry (SI) (Curtis et al. 2006; Wapenaar et al. 2010), roadside passive MASW (Park et al. 2008; Humire et al. 2015), and the multichannel analysis of passive surface waves (MAPS) (Cheng et al. 2016; Ning et al. 2021). Their ultimate goal is to obtain subsurface S-wave velocities from continuous noise recordings and further delineate underground structures.

In general, passive surface-wave data are usually recorded over a long time, from several months to years. Previous studies demonstrated that temporal averaging over long-period seismic noise data can attenuate the azimuthal effects of noise sources (Shapiro and Campillo 2004) and make the effective distribution of noise sources nearly homogenous (e.g., Snieder 2004; Lin et al. 2008), which fulfills the requirements for the stationary-phase assumption (Sabra et al. 2005; Stehly et al. 2006). Long-period observations of noise data, however, are often associated with higher costs and may be difficult to carry out in highly populated urban areas. Some strategies (e.g., Afonin et al. 2019; Song et al. 2021; Xu et al. 2021) were proposed to improve signal-to-noise ratio (SNR) of the retrieved surface waves and achieve reliable surface-wave dispersion measurements in the condition of shorter recording time, such as the eigenvalue-based processing method (Menon et al. 2012; Seydoux et al. 2017; Wu et al. 2020), the SNR stacking (Cheng et al. 2015; Xie et al. 2020), a phase-weighted stack method (Schimmel et al. 2011; Cheng et al. 2021a), the data selection methods (Cheng et al. 2018, 2019; Pang et al. 2019), and the multichannel-coherency-weighted stack method (Liu et al. 2021). Short-period noise data acquisition not only greatly reduces costs and improves efficiency of field work, but also has potential for real-time monitoring in urban areas.

Numerous time-window processing techniques were introduced to enhance SNR of noise cross-correlation function (NCF) and resolution of surface-wave dispersion image. These techniques include the length selection of time window (Groos et al. 2012; Seats et al. 2012; Zhang et al. 2019), short time-window stacking (Prieto et al. 2011), and asymmetry-based data selection (Zhou et al. 2018). The effects of directional noise sources, however, were not considered in these above-mentioned researches. To avoid the effects caused by the directional noise sources and obtain an unbiased dispersion energy of surface waves, various data- and array-based solutions have been proposed by many researchers. For example, the three-component noise data are rotated to force each station pair to realign in the noise direction (Roux 2009). In addition, the noise data from the receiver array are selected as a result of the orientation of array aligning with the direction of noise source distribution (Guan et al. 2021). Le Feuvre et al. (2015) introduced the use of beamforming performed with cross-correlations for constraining the directionality of noise and reducing the effects of aliasing. However, this method still depends on 2D arrays for good results. On the basis of 1D linear arrays, Cheng et al. (2016) proposed the MAPS method by adjusting the azimuth of noise sources. Compared to the 1D linear array, 2D arrays are relatively difficult and inconvenient to lay out in the residential areas. The 2D arrays may not be suitable for deploying in urban environments, although they have been used to accurately determine the noise source azimuth (Strobbia and Cassiani 2011; Nakata 2016) and remove ambiguities of the directionality of noise (Park and Miller 2008; Halliday et al. 2008). Therefore, Liu et al. (2020) suggested that adding two off-line receivers to a conventional linear array to form a pseudo-liner array can increase the azimuthal coverage to obtain unbiased dispersion image. In the passive surface-wave surveys, the distribution of traffic-induced noise changes with time, the propagation direction of waves is not always along the linear array, and the data acquisition is relatively short for near-surface applications. These challenges undoubtedly place higher demands on passive surface-wave processing methods.

Due to complex cultural activities in urban areas, noise sources are not randomly distributed in time and space, resulting in the overestimated phase velocities (Asten and Hayashi 2018). In this study, we propose a new selection scheme based on stationary-phase zones for retrieving high-frequency (approximately > 1 Hz) surface waves, since man-made activities are the dominant influence in urban environments. We

perform a beamforming algorithm based on a pseudo-linear array on each ultrashort segment due to the noise source distribution changing in a short time. The azimuthal range of in-line noise sources is combined with a desired range of velocity to select qualified segments, whose azimuth is determined by the first Fresnel angle calculated from the measured shortest wavelength. By searching for the peak of each segment beamforming output, the dominant azimuth and phase velocity of noise sources are obtained. According to the constrained conditions that include the azimuthal range of in-line noise sources and a desired range of velocity, we select these segments with positive contributions to recover surface waves. Firstly, the conventional passive surface-wave methods (i.e., seismic interferometry (SI), refraction microtremor (ReMi) and roadside passive MASW) are reviewed; and the processing procedure of our proposed scheme is presented. Secondly, we use a synthetic test and two real-world examples to prove the superiority of our selection scheme over the conventional passive surface-wave methods. Finally, the advantages and limitations of the selection scheme are briefly discussed, and several conclusions are presented.

2 Methods and Data Processing

2.1 Seismic Interferometry Method

Previous researchers (Weaver and Lobkis 2004; Roux et al. 2005; Sabra et al. 2005) have shown that under a homogeneous source distribution assumption, empirical Green's functions (EGFs) are obtained by taking the time derivative from the NCF, which are equivalent to real Green's function except for a frequency-dependent amplitude correction. Assuming receivers are located at positions A and B, the relationship between them can be expressed as:

$$\frac{dC_{AB}(t)}{dt} \approx -G_{AB}(t) + G_{BA}(-t), -\infty \le t \le \infty \tag{1}$$

where $C_{AB}(t)$ is the cross-correlation between two receivers A and B, $G_{AB}(t)$ denotes the actual Green's function at receiver B for a virtual source excited at receiver A, and $G_{BA}(-t)$ is the time-reversed Green's function at A for a virtual source excited at B. Formula (1) is also equivalent to:

$$G_{AB}(t) = -\frac{dC_{AB}(t)}{dt}, 0 \le t \le \infty \tag{2}$$

$$G_{BA}(t) = -\frac{dC_{AB}(-t)}{dt}, 0 \le t \le \infty \tag{3}$$

Due to the spatial reciprocity of the Green's functions, $G_{AB}(t)$ is equal to $G_{BA}(t)$. The causal and acausal parts of cross-correlations are averaged to achieve the symmetric correlation function that is used to obtain the final evaluated Green's function. In most cases, this increases the SNR and also effectively reduces the azimuthal effect of the directional noise sources (Bensen et al. 2007; Wu et al. 2020). In the real world, the single directional noise sources are common in urban areas. Our scheme would

focus on processing noise data with in-line noise sources coming from one end of the receiver array. Here, the in-line noise source distribution does not satisfy the SI requirement that noise sources be randomly distributed around the array, there is a $\pi/4$ phase shift between the EGF and the NCF (Lin et al. 2008). The phase difference, however, does not affect the correctness of the phase velocity measurements because the phase-shift method (Park et al. 1998) uses the relative difference in phase travel time.

2.2 Refraction Microtremor Method

The ReMi method proposed by Louie (2001) assumed that the incident surface waves propagate along a linear array, and its basis is taken from the τ-p transform in the active surface-wave methods. In the dispersion energy measurements, Louie (2001) applied the τ-p transform in forward and reverse along the linear array. The expression of the ReMi method can be written as:

$$E(f,|p|) = \left|e^{\phi_0}\right| * \left(\left| \sum_{j=1}^{N} e^{j2\pi(p-p_0)x_j} \right| + \left| \sum_{j=1}^{N} e^{-j2\pi(p+p_0)x_j} \right| \right) \tag{4}$$

where ϕ_0 is the initial phase, N represents the number of stations, and p_0 is the surface-wave slowness at frequency f. Due to the lack of knowledge about the distribution of noise sources, the "crossed" artifacts (Xu et al. 2017; Cheng et al. 2018) would exist in the ReMi measurement using a bidirectional velocity scan process. The "crossed" artifacts contaminate the true surface-wave dispersion energy at high frequencies (Xi et al. 2021).

2.3 Roadside Passive MASW Method

Park et al. (2008) developed the roadside passive MASW method that used phase-shift method to process the passive surface-wave data from nearby traffic. Similar to the ReMi method, both the forward and reverse directional velocities ($\pm v$) are considered to scan at the slant-stacking procedure:

$$E(f,v) = \left|e^{\phi_0}\right| * \left(\left| \sum_{j=1}^{N} e^{j2\pi f(v-v_0)x_j} \right| + \left| \sum_{j=1}^{N} e^{-j2\pi f(v+v_0)x_j} \right| \right) \tag{5}$$

where v_0 is the surface-wave phase velocity at frequency f. During the noise data process, the dispersion images are stacked together to improve the image resolution. However, the "crossed" artifacts (Cheng et al. 2018) are also presented in the roadside passive MASW measurement and affect the extraction of surface-wave dispersion curves (Dai et al. 2018). Moreover, dispersion images generated using noise data may not necessarily be correct because of the azimuthal effects from off-line noise sources located outside of the first Fresnel zone, especially in complex urbanized environments. Therefore, proposing a segment selection based on noise source distribution is important to obtain accurate phase velocities.

2.4 Beamforming Analysis

In highly populated urban areas, unevenly distributed noise sources are caused by human activities. In addition, the recording time of noise data is relatively short for near-surface applications. It is necessary to analyze noise source distribution changing with time. So, we apply a beamforming algorithm to analyze each ultrashort (e.g., 30 s; 60 s) segment and select those segments affected by in-line noise sources. The equation of the array beamforming (Rost and Thomas 2002; Liu et al. 2020) can be presented as:

$$B(w, \theta, v) = \left| \frac{1}{N} \left(\sum_{j=1}^{N} \frac{e^{-iw\tau_j(\theta,v)} r_j(w)}{\left| r_j(w) \right|} \right) \right|^p \tag{6}$$

where $i = \sqrt{1}$, w denotes the angular frequency, θ and v are the scanning angle and velocity, respectively, $\tau_j(\theta, v) = x_j cos(\theta)/v + y_j sin(\theta)/v$ is the time delay between the receiver array center located at origin (0, 0) and the jth receiver located at (x_j, y_j), $r_j(w)$ is the record of the jth receiver in the frequency domain, and p denotes the power factor, usually set to 1 or 2.

We take the same strategy as introduced in Liu et al. (2020) by adding two off-line receivers to a conventional linear array (i.e., a pseudo-linear array). Similarly, we compare the difference of beamforming resolution calculated from a pseudo-linear array to the result from a linear array in the following field tests. The array response function (ARF) is calculated by:

$$\text{ARF}(w, v, \theta) = \left| \frac{1}{N} \left(\sum_{j=1}^{N} e^{-iw\left(x_j\cos(\theta)/v + y_j\sin(\theta)/v\right)} \times e^{iw_0\left(x_j\cos(\theta_0)/v_0 + y_j\sin(\theta_0)/v_0\right)} \right) \right|^p \tag{7}$$

where w_0 and v_0 are the angular frequency and velocity of the plane wave, respectively, the azimuth θ_0 is the angle of the incident plane-wave front arriving at the array. The power factor p is set as 1 in the subsequent sections.

2.5 Data Processing

For processing noise data, the proposed a beamforming-based segment selection scheme is shown in Fig. 1a. Similar to the procedures introduced in Bensen et al. (2007), firstly, the noise data are divided into ultrashort segments such as seconds or minutes. Secondly, the de-meaning and de-trending are utilized to these segments. Then, we apply the beamforming algorithm based on a pseudo-linear array to each segment and capture the dominant azimuth of noise sources. Here, we calculate the Fresnel angle θ_F (Sadeghisorkhani et al. 2017) to describe the first Fresnel zone (the shaded regions in Fig. 1b) for incoming plane waves from a distance,

$$\theta_F = \sqrt{\frac{\lambda}{2L}} \tag{8}$$

where L is the interstation distance, and λ denotes the wavelength of a plane wave. In near-surface applications, L represents the distance between two receivers located at both ends of the array, i.e., the receiver spread. The phase velocity in higher frequencies is relatively

(a)

(b)
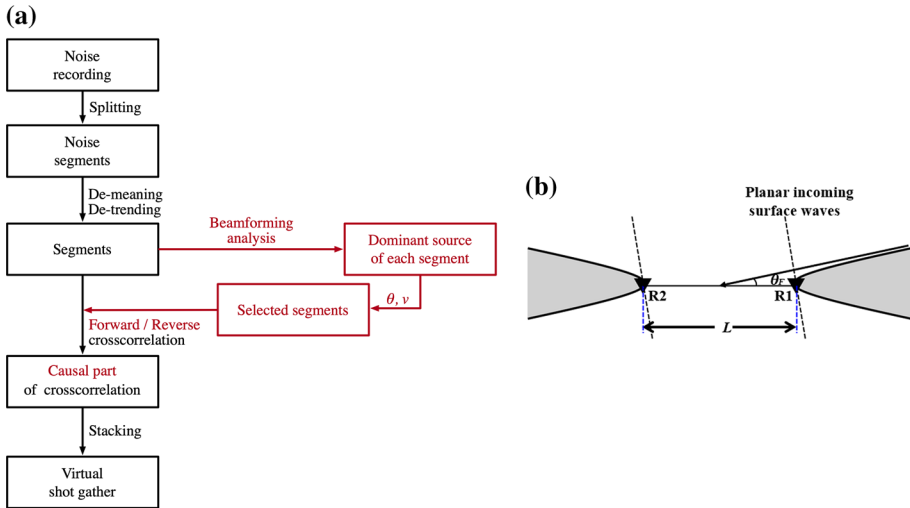
Fig. 1 **a** The workflow of the proposed scheme for processing ambient seismic noise. The red parts denote the selection scheme adding to the conventional process. θ and v represent the dominant azimuth of noise sources and the phase velocity of the plane waves obtained from the beamforming output of each segment, respectively. **b** A schematic diagram showing planar waves propagating between two receivers R1 and R2, and defining the symbols used in formula (8). θ_F denotes the Fresnel angle. L stands for the interstation distance. The region of constructive interference is represented by the shaded regions

accurate even in the existence of off-line noise sources [this phenomenon can be found in Xu and Mikesell (2017), Xu et al. (2017) and Zhou et al. (2018)] due to the rapid oscillation of cross-correlations in the non-stationary-phase zone. Thus, we take the phase velocity at a higher frequency to obtain the measured shortest wavelength and determine the first Fresnel angle. In the first Fresnel zone (Fig. 1b), the constructive interference will occur between two stations whose noise recordings contribute to retrieve surface waves by cross-correlations. The segment is selected if the dominant azimuth and the phase velocity obtained from the peak on the beamforming output meet the constrained conditions, which are the azimuthal range of in-line noise sources and a desired range of surface-wave phase velocity.

In order to introduce fewer nonphysical biases in cross-correlation, the temporal and spectral normalization techniques are not used in a synthetic test, and only the temporal normalization (i.e., one-bit) is applied to the real-world examples. Then, the cross-correlation is performed on the preprocessed segments. According to the location of the dominant noise source, the order of cross-correlation can be determined, that is, the forward (the first trace as the virtual source and the others as receivers) or the reverse (the last trace as the virtual source and the others as receivers) cross-correlation is determined. The physical meaning is that the station closest to the dominant noise source is chosen as the virtual source to be cross-correlated with other stations. Thus, the causal parts of cross-correlations are stacked to obtain the final virtual shot gather rather than stacking of the causal and acausal parts. The surface-wave dispersion image is produced by the phase-shift method.

3 A Synthetic Test

To test the feasibility of our selection scheme for short-period seismic noise data, we simulated the 30-min noise data affected by different distributions of noise sources. We first calculated the theoretical dispersion curve of the Rayleigh-wave fundamental mode from the initial model (Table 1). Only the vertical-component noise data were generated by following the numerical method introduced in Lawrence et al. (2013). The noise source is described by a 15 Hz Ricker wavelet. The quality factor Q is set as infinite to take no account of attenuation between different frequencies. To mimic the noise distribution in urban environments, we designed the distributions of noise sources (blue dots in Fig. 2a), that 500 in-line noise sources are randomly distributed at polar coordinates between R_1 = 1 km, $\theta_1 = -15$ ° and $R_2 = 2$ km, $\theta_2 = 15$ °, and 1000 off-line noise sources with the same radius are randomly distributed at polar coordinates between $\theta_3 = 45$ ° and $\theta_4 = 75$ °. Twenty-four geophones are deployed on 2-m intervals along the horizontal direction and two off-line receivers with a 13-m interval are located at one side of the receiver array (Fig. 2b). In our test, the in-line and off-line noise sources are randomly activated with a 30-s duration. Nevertheless, the noise sources in the real world are complex, we would further test the feasibility of our selection scheme by two real-world examples as presented in latter sections.

As an example, we showed a 30-s segment of synthetic noise data from 24 channels along the horizontal direction (Fig. 2c). The surface-wave wavelength λ is obtained by the theoretical phase velocity of each frequency and the Fresnel angle is determined. Figure 3a shows the hyperbolas for different frequencies. The wavelengths are approximately proportional to the Fresnel angle (Fig. 3b). We took the wavelength at 30 Hz to calculate the Fresnel angle, in order to determine the azimuthal range of in-line noise sources. In this case, the first Fresnel angle is equal to 15.5 °. Here, the azimuths of 0 ° and 90 ° correspond to the true east and north, respectively. That is, the direction of the tested array is from east (0 °) to west (180 °). Thus, the azimuthal range of in-line noise sources is from −15.5 ° to 15.5 °, or from 164.5 ° to 195.5 °.

During the processing of noise data, we followed the workflow as shown in Fig. 1a. The beamforming using a pseudo-linear array was performed on each segment to locate the noise sources. The only one peak (the maximum value in the 2D power spectrum matrix $(\theta-v)$, see Fig. 4) on the beamforming output can be searched for a given frequency band from 5 to 30 Hz. Figure 4 displays the results of the beamforming outputs obtained from different noise datasets. Figure 4a shows the average azimuth of noise source distribution during the entire observation period, with the peak in the sources at 54 ° azimuth with a phase velocity of 230 m/s. This azimuth just represents the average azimuthal effect on all time and is unable to accurately indicate the dominant azimuth of in-line or off-line noise sources. Figure 4b reveals the noise source distribution of one 30-s segment affected by in-line noise sources, with the only peak in the sources at 355 ° azimuth with a phase velocity of 234 m/s. Another type of noise sources—off-line noise sources—can be easily seen in Fig. 4c, with only peak in the sources at 60 ° azimuth with a phase velocity of

**Table 1** Physical parameters of a two-layer earth model

Layer number	V_S(m/s)	V_P(m/s)	ρ(kg/m^3)	Thickness (m)
1	220	380	2000	10
2	440	760	2000	Infinite
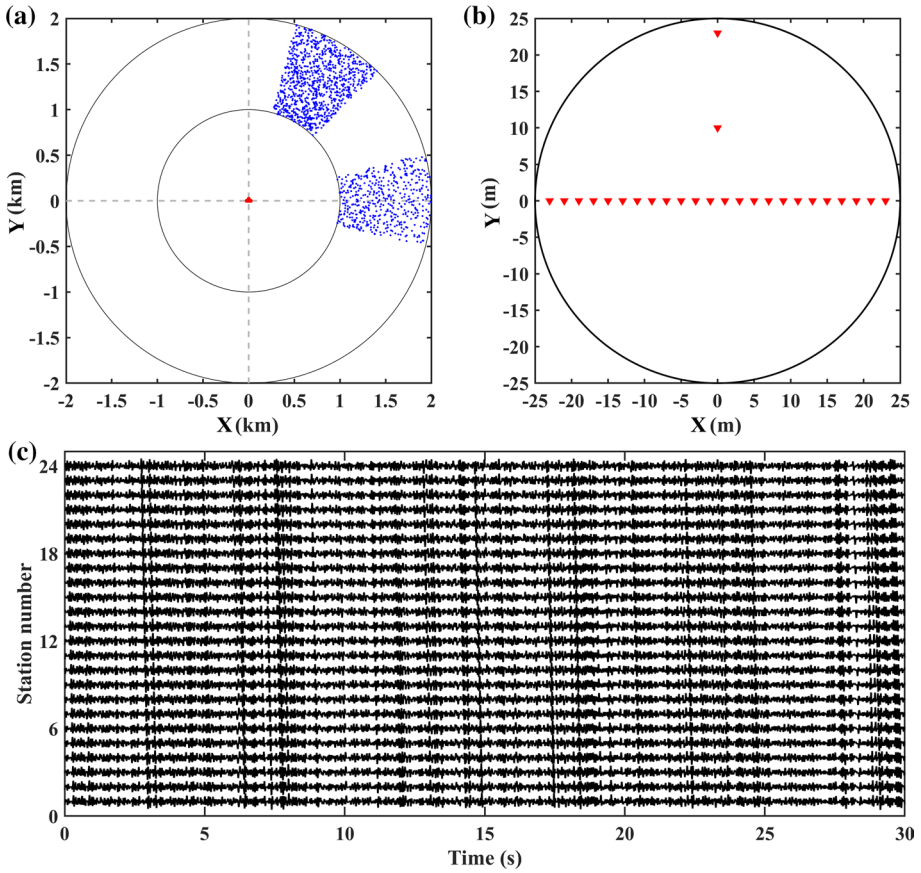
Fig. 2 The geometries of **a** noise source (blue dots) distribution and **b** receiver array with two off-line receivers (red triangles). **c** One 30-s segment of the 24-channel synthetic noise recordings along the horizontal direction
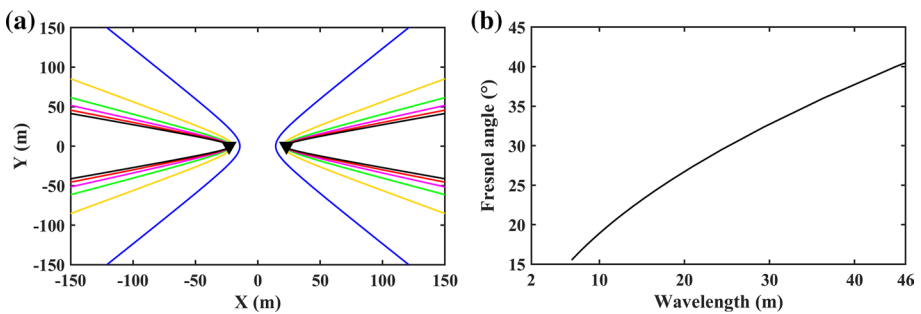
Fig. 3 **a** The hyperbolas for different frequencies 5 Hz (blue), 10 Hz (yellow), 15 Hz (green), 20 Hz (magenta), 25 Hz (red), and 30 Hz (black). The solid black triangles denote the receivers located at both ends of the array along the horizontal direction. The distance between two receivers is 46 m. **b** The relationship between the Fresnel angles and the wavelengths, where the range of wavelengths is limited to 2 m (the receiver interval) to 46 m (the receiver spread)
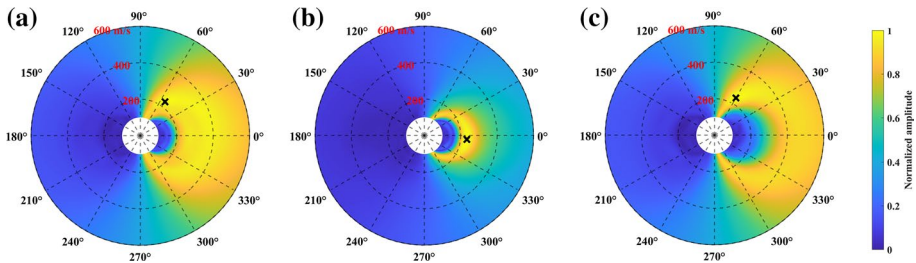
Fig. 4 Beamforming outputs from **a** all segments, **b** one 30-s segment affected by in-line noise sources, and **c** another 30-s segment affected by off-line noise sources in the frequency band from 5 to 30 Hz, respectively. The black crosses as shown in **a-c** denote the unique peaks on the beamforming outputs, which are in the sources at 54 °, 355 °, and 60 ° azimuths, and the corresponding phase velocities of 230 m/s, 234 m/s, and 235 m/s, respectively

235 m/s. These results indicate that it is essential to analyze the noise source distribution of each segment. Meanwhile, we designed the desired range of surface-wave phase velocity from 100 to 400 m/s by referring to the noise energy distribution of the beamforming output or the theoretical dispersion curve. The segment will be selected if the peak with two parameters (i.e., noise source azimuth and phase velocity) meets the constrained conditions. Finally, the causal parts of cross-correlations generated from selected segments are stacked to generate the final virtual shot gather.
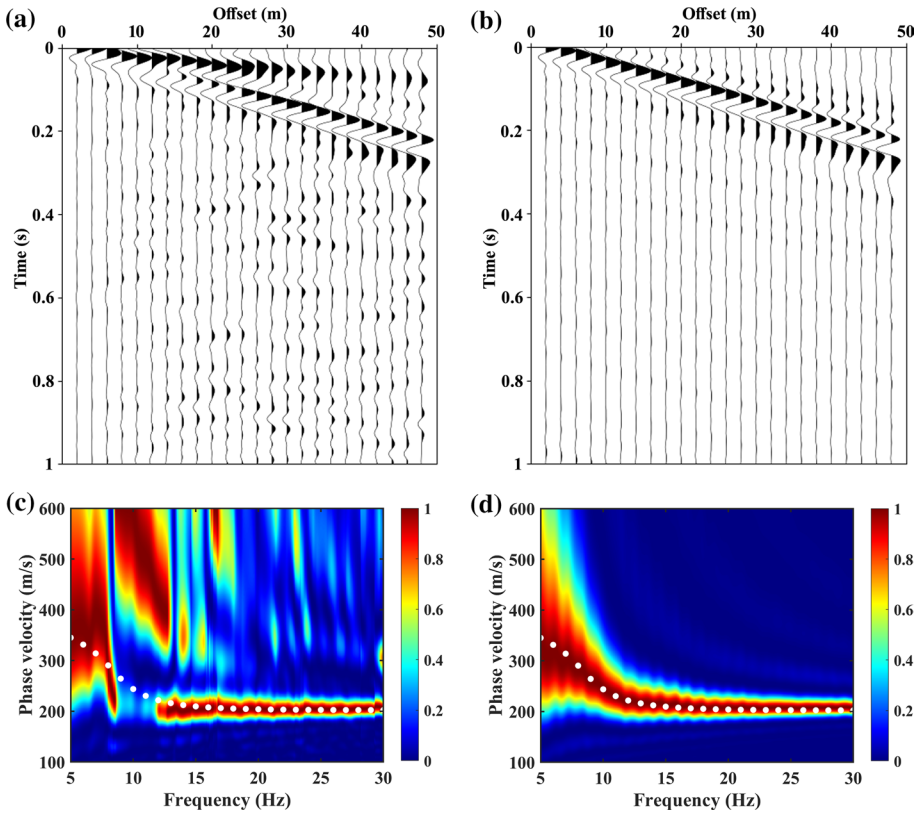
The virtual shot gathers and dispersion images generated from different datasets are shown in Fig. 5. The SNR (6.97) of the virtual shot gather using all segments (Fig. 5a) is lower than that (16.79) of the virtual shot gather using selected segments (Fig. 5b), and the corresponding dispersion image (Fig. 5c) also performs worse than that in Fig. 5d, especially in the lower-frequency range (i.e., < 12 Hz). These results indicate that the virtual shot gather generated using selected segments affected by in-line noise sources has a higher SNR. Removal of these segments affected by off-line noise sources is beneficial to image higher-resolution dispersion energy, because the existence of these off-line noise sources would result in inaccurate cross-correlation functions and overestimated phase velocities in lower frequencies.

4 Two Real-World Examples

To further test the validity of our new segment selection scheme (Fig. 1a) with traffic-induced noise in urban environments, we present two real-world cases.

4.1 Case 1: Hangzhou

The experiment was carried out in the city of Hangzhou, China (Fig. 6a). The survey line was located in an abandoned parking lot, surrounded by some roads. The orientation of the survey line is from northwest to southeast, and the corresponding azimuth is from 162.2° to 343.2°. To better couple the geophones with the ground, we drilled holes (represented by the red box in Fig. 6b) to deploy the geophones in the soil before field work. Twenty-seven Fairfield Nodal three-component geophones (red dots in Fig. 6a) with a 5 Hz dominant frequency were deployed at 5-m intervals. S-wave velocity measurements in a borehole

Fig. 5 Virtual shot gathers and dispersion images of surface waves calculated from 24 channels along the horizontal direction. The results in **a** and **c** are calculated from all segments. The results in **b** and **d** are obtained using selected segments affected by in-line noise sources. The white dots represent the theoretical dispersion curve of Rayleigh-wave fundamental mode

(a black cross approximately 0.4 m away from the survey line in Fig. 6a) were obtained, to verify the inverted results. Here, only the vertical-component noise data were used for the real-world test. According to the strategy introduced in Liu et al. (2020), we added two off-line receivers (blue dots in Fig. 6a) with 10-m intervals to one side of the survey line to form a pseudo-linear array, for increasing the azimuthal coverage. The traffic-induced noise data were recorded with a sampling frequency of 500 Hz from the local time 19:00 on June 1 to 17:30 on June 2, 2020. Figure 7a exhibits an example of 30-s segment. The average power spectrum from traces 1–27 reveals that the traffic-induced noise data have a peak frequency for surface waves of approximately 10 Hz with a frequency band of 2 to 15 Hz (Fig. 7b). The SI method was used to process the noise data. The cross-correlation (Fig. 7c) with a weak symmetry indicates that the dominant energy comes from the southeast.

From the result in Fig. 7c, we obtained the dispersion image of surface waves (Fig. 8a) obtained using the SI method for comparison with that generated using the ReMi (Fig. 8b) and roadside passive MASW (Fig. 8c) methods. Similarly, the same preprocessing procedures including de-meaning, de-trending, and the temporal (i.e., one-bit) normalization were also performed for segments with the same length when using the ReMi and roadside
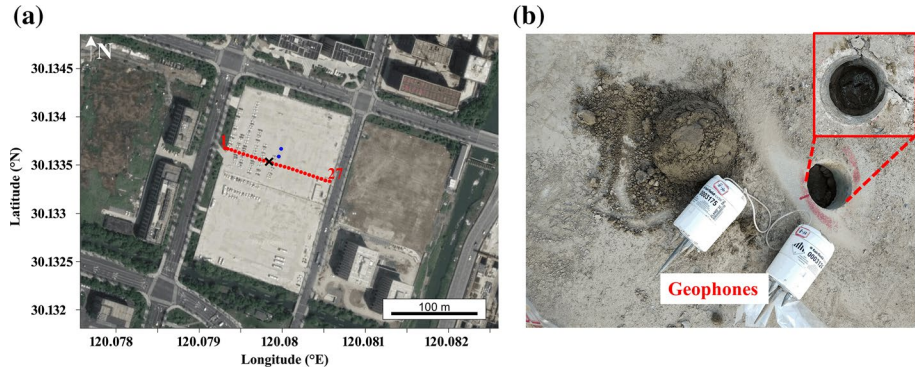
Fig. 6 **a** A satellite photograph of the survey line with 27 in-line (red dots) and 2 off-line receivers (blue dots) that were deployed at the obsolete parking lot in the Yunqi town, Hangzhou, China. The interval of the linear array numbered 1 to 27 is 5 m, and the interval between two off-line receivers is 10 m. The borehole is located approximately 0.4 m away from the survey line, represented by a black cross. **b** Geophones were deployed in the holes (enlarged view at the top right-hand corner, represented by red box) with a width of 10 cm and a depth of 20 cm
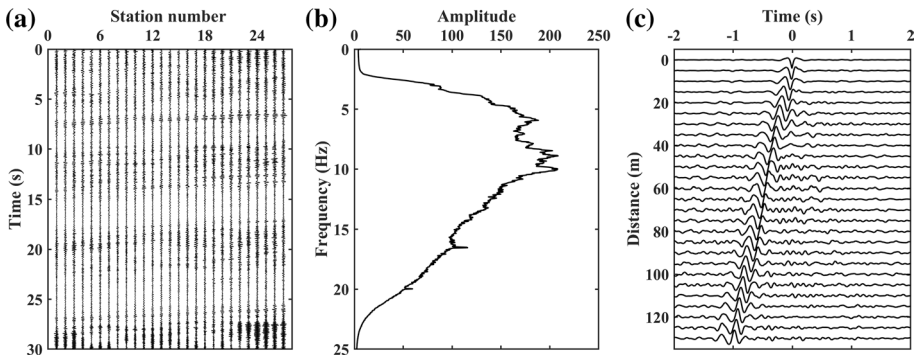

Fig. 7 **a** One 30-s segment of observed traffic-induced noise data (traces 1–27). **b** The average power spectrum of noise recordings generated from the traces 1–27. **c** A cross-correlation gather calculated from all noise data
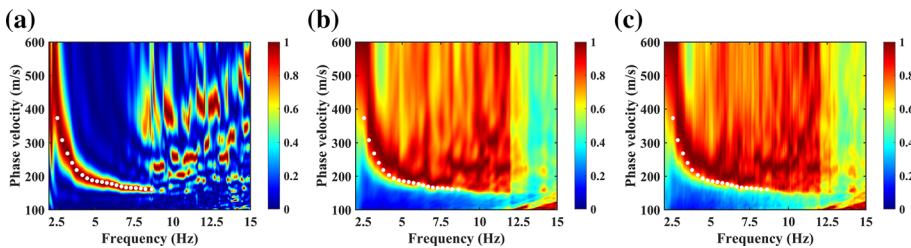

Fig. 8 Comparison of dispersion images calculated from **a** stacking the acausal and causal parts of cross-correlations, using the **b** ReMi and **c** roadside passive MASW methods. The white dots in **a**–**c** represent the extracted dispersion curve by tracing the peak values of dispersion energy in **a**

passive MASW methods. We extracted the dispersion curve (white dots in Fig. 8a) by tracing the high-energy concentration on the dispersion image, from 2.6 to 8.6 Hz. To compare the quality of the dispersion images from these methods, the dispersion curve in Fig. 8a is overlain on the dispersion images in Fig. 8b, c. The dispersion energy trend of the fundamental mode in Fig. 8a is more continuous than that in Fig. 8b, c. The SI method stacks all cross-correlations and the dispersion image is obtained by only one transformation. This attenuates less coherent signals and increases the SNR of the virtual shot gather. The ReMi and roadside passive MASW methods stack all dispersion images generated by raw noise data and use a bidirectional velocity scan process, resulting in "crossed" artifacts (Xu et al. 2017; Cheng et al. 2018) as shown in bottom left corner of Fig. 8b, c. Figure 9a presents the hyperbolas for different frequencies. Figure 9b indicates that the Fresnel angle increases with the wavelength. Considering the accurate phase velocities at relatively higher frequencies, we defined the azimuthal range of in-line noise sources by calculating the first Fresnel angle (i.e., 15.3°) at 8.6 Hz. Therefore, the azimuthal range of in-line noise sources is from 146.9° to 177.5° or from 326.9° to 357.5°.

We calculated the ARF between the linear (Fig. 10a) and pseudo-linear (Fig. 10b) arrays to assess their ability to capture the correct source azimuth. Given a plane wave with a frequency of 15 Hz, a velocity of 400 m/s, and an azimuth of 45°, the ARF results of two arrays are obtained by formula (7) as shown in Fig. 10c, d. The result in Fig. 10c indicates that the noise source azimuth cannot be accurately estimated using the linear array. Nevertheless, the pseudo-linear array can indicate the correct characteristics of a plane wave, showing only one peak in Fig. 10d. The results in Fig. 10 demonstrate that the pseudo-linear array can capture the accurate azimuth of noise sources with the ARF. We applied beamforming to analyze the noise source distribution of each segment in the frequency band from 2 to 15 Hz. Figure 11a displays the phase velocities and the dominant azimuths of noise sources from the peaks on the beamforming outputs in all segments. The desired range of surface-wave phase velocity is determined by the raw dispersion results (Fig. 8), i.e., from 100 to 600 m/s. Therefore, the constrained conditions including the azimuthal range of in-line noise sources and a desired range of surface-wave phase velocity are remarked by the dashed boxes in Fig. 11a. Figure 11b reveals the average azimuth of noise sources from all segments, with a dominant azimuth in 330°. However, this average azimuth is unable to accurately describe the noise source azimuth in different times,
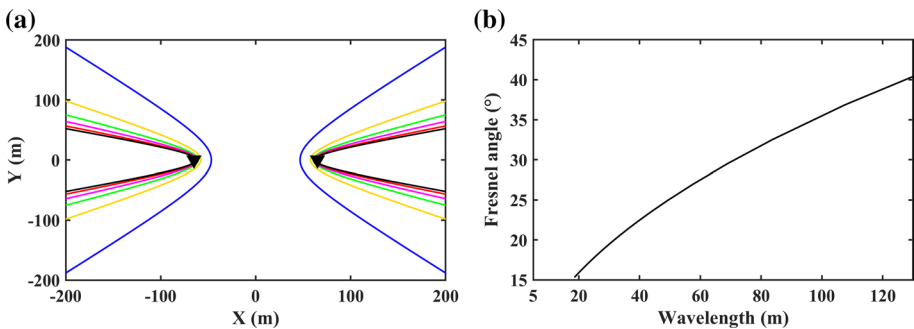

Fig. 9 a The hyperbola for different frequencies 2.6 Hz (blue), 3.8 Hz (yellow), 5.1 Hz (green), 6.4 Hz (magenta), 7.6 Hz (red), and 8.6 Hz (black). The solid black triangles denote the receivers located at both ends of the array, in the 2D Cartesian coordinate system. The distance between two receivers is 130 m. **b** The relationship between the Fresnel angles and the wavelengths, where the range of wavelengths is limited to 5 m (the receiver interval) to 130 m (the receiver spread)
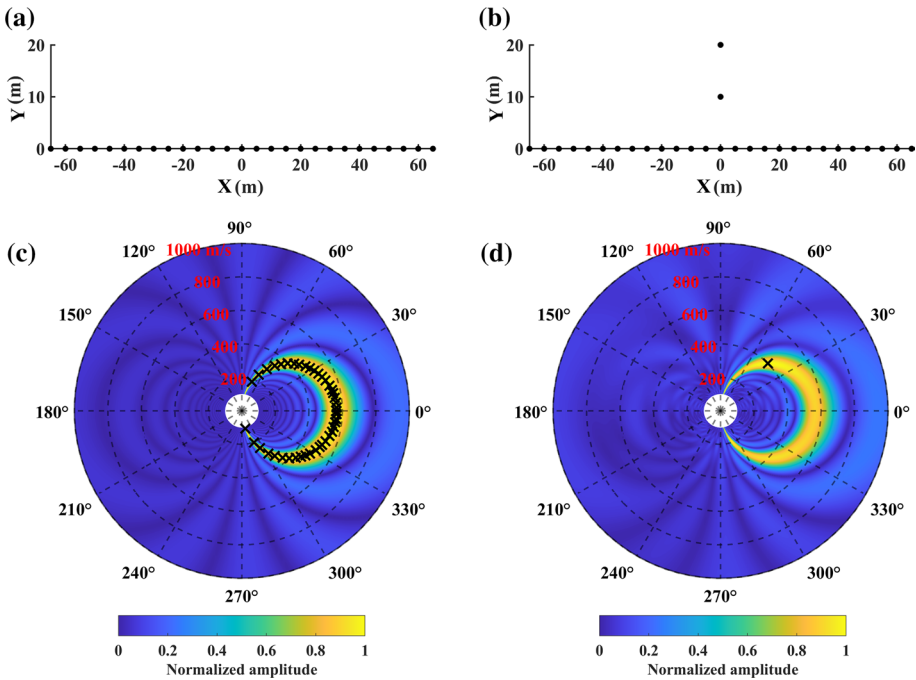
Fig. 10 The geometry of **a** a linear array and **b** a pseudo-linear array. Given a plane wave with a frequency of 15 Hz, a velocity of 400 m/s and an azimuth of 45°, the ARFs of the linear and the pseudo-linear arrays shown in **c** and **d**, respectively. The black dots in **a** and **b** denote the receivers on the linear and pseudo-linear arrays. The black crosses in **c** and **d** represent the peak values on the contour map

especially in densely populated urban areas. We showed two 30-s segments affected by in-line noise sources picking from the dashed boxes in Fig. 11a. The dominant azimuth in Fig. 11c is different from that in Fig. 11b, d.

As mentioned in the previous paragraph, we selected the segments when the phase velocity and the dominant azimuth meet the constrained conditions. We calculated the cross-correlations of these selected segments. The final virtual shot gather was generated by stacking the causal parts of the cross-correlations from selected segments. We compared the virtual shot gather calculated from selected segments to the result from all segments (Fig. 12). The SNR (10.02) of the virtual shot gather in Fig. 12b is higher than that (8.14) in Fig. 12a. The dispersion image in Fig. 13 is generated from the virtual shot gather in Fig. 12b, which shows continuous and very well-defined fundamental and first higher modes of Rayleigh-wave energy from 2.6 to 14.9 Hz. Compared to the dispersion image in Fig. 8a, the dispersion image in Fig. 13 has more phase velocities in the frequency band from 8.6 to 14.9 Hz and possesses higher resolution in the frequency–velocity (*f*–*v*) domain. We inverted the dispersion curves extracted from Fig. 8a and Fig. 13 and obtained the S-wave velocities (Fig. 14). According to the borehole measurements, we defined the initial model presented in Table 2. The S-wave velocity model generated using all segments converged in two iterations, the root-mean-square (RMS) error is reduced from 39.68 to 3.35 m/s (Fig. 14a). The S-wave velocity model obtained from selected segments converged in one iteration, the RMS error is
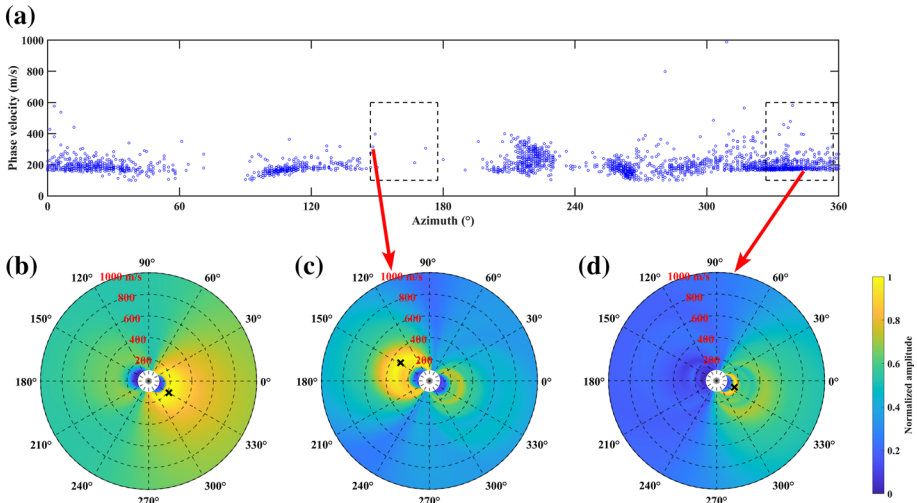
Fig. 11 **a** The values (blue circles) about the dominant azimuth of noise sources and the phase velocity obtained from the beamforming output of each segment. The black dashed boxes represent the constrained conditions. In the frequency band of 2 to 15 Hz, beamforming outputs from **b** all noise data, **c** a 30-s segment affected by in-line noise sources located at the head of the survey line, and **d** another 30-s segment affected by in-line noise sources located at the end of the survey line. The black crosses as shown in **b**–**d** denote the peaks on the beamforming outputs, which are in the sources at 330°, 148°, and 340° azimuths, and the corresponding phase velocities of 261 m/s, 315 m/s, and 175 m/s, respectively
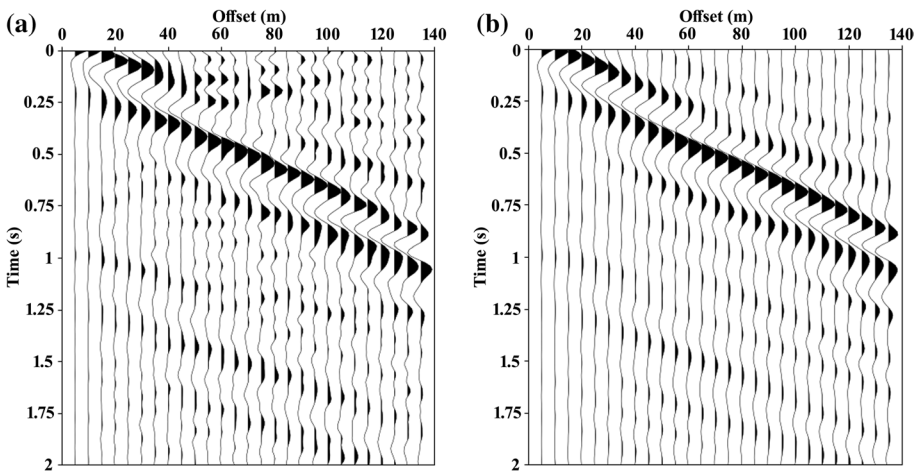
Fig. 12 The virtual shot gathers are generated from the **a** full and **b** selected noise data, respectively

dropped from the initial RMS error of about 28.58 to 4.76 m/s (Fig. 14b). Neverthe-
less, the measured dispersion curves and the dispersion curves calculated from inverted
models 1 and 2 reveal are in good agreement (Fig. 14a, b). The inverted model from
selected segments is more consistent with the borehole S-wave velocity measurements
than that from all segments, especially in the depth less than 22 m. More phase veloci-
ties in the higher frequency band obtained from selected segments make the inversion

Fig. 13 The dispersion image of surface waves is calculated from the virtual shot gather shown in Fig. 12b. The white dots represent the extracted dispersion curves by tracing the peak values of dispersion energy
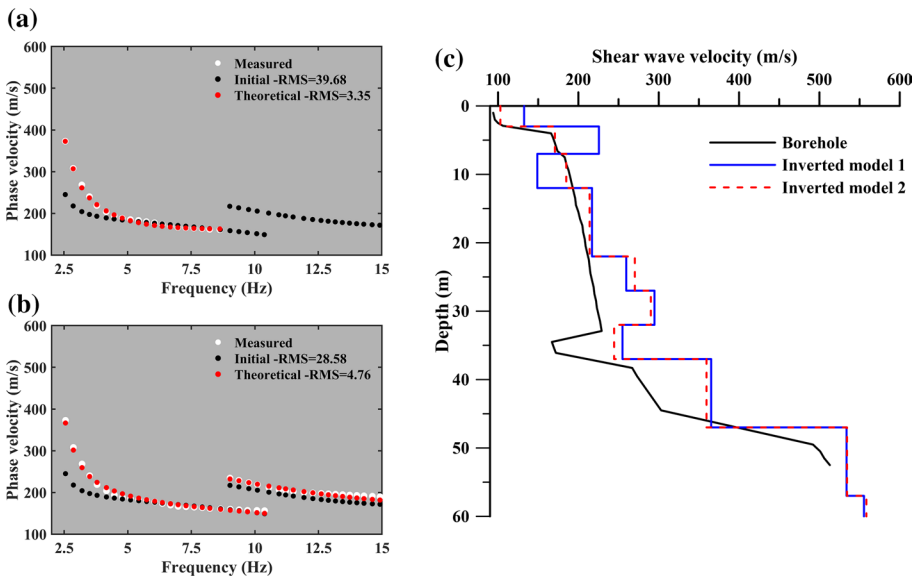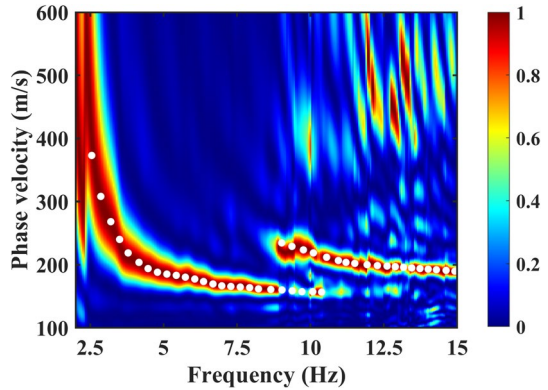
Fig. 14 **a** and **b** Comparison of the measured dispersion curves (white dots) obtained using all and selected segments with the theoretical dispersion curves (red dots) calculated from the inverted models 1 and 2, respectively. The black dots denote the theoretical dispersion curve of the initial model (Table 2). **c** Comparison of the inverted models 1 (solid blue line) and 2 (dashed red line) with the borehole measurements (solid black line). The inverted model 1 was obtained by inversion of the fundamental mode (white dots in **a**) only. The inverted model 2 was generated by inversion of the fundamental and first higher modes (white dots in **b**) simultaneously

system stable and the inversion result close to the real model of subsurface structures, especially at shallower depths.

4.2 Case 2: Wuhan

The experiment was carried out in the city of Wuhan, China (Fig. 15a). Fifty-two three-component geophones with a 5 Hz dominant frequency were deployed close to Hanshui

**Table 2** Physical parameters of a ten-layer earth model

Layer number	V_S(m/s)	V_P(m/s)	ρ(kg/m^3)	Thickness (m)
1	95	225	1850	3
2	170	458	1870	4
3	193	520	1920	5
4	210	565	1950	10
5	220	590	1980	5
6	230	620	1990	5
7	170	457	1872	5
8	306	824	2000	10
9	520	1400	2010	10
10	550	1480	2100	Infinite

Park. Here, two off-line receivers were located 2 m and 16 m away from the survey line (Fig. 15b), respectively. Geophones 1–50 were deployed at 2-m intervals and the noise data from these geophones were used to further evaluate the validity of the proposed scheme. The orientation of the linear array is from southeast to northwest, and the corresponding azimuth is from 349.2° to 169.3°. The traffic-induced noise data were recorded with a sampling frequency of 500 Hz from local time 12:00–16:00 on 10 November 2020. In this test, we only utilized the vertical-component noise data to obtain Rayleigh waves. We split the 4-h continuous noise data into 240 slices of a 60 s time window without overlap, an example of 60 s time windowed record is presented in Fig. 16a. Figure 16b illustrates the average power spectrum from traces 1–50, which indicates that the signal spreads over the frequency band of 5 to 20 Hz, with a peak frequency of 10.5 Hz. The scheme (Fig. 1a) was used to process traffic-induced noise data.

Figure 17a presents the virtual shot gather generated from all segments. Its corresponding dispersion image is shown in Fig. 17b. The measured dispersion curve was obtained by tracing the dispersion energy from 9.8 to 19.1 Hz. Note that the same preprocessing procedures were also performed on all segments with the same length when using the ReMi and roadside passive MASW methods. We applied the ReMi and
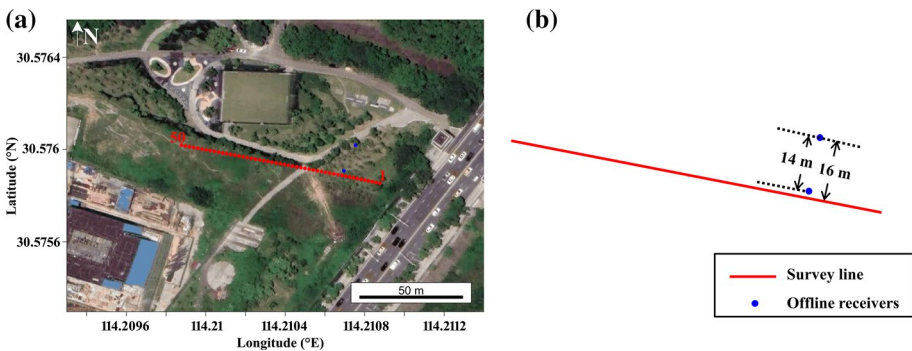
Fig. 15 a A satellite photograph of the survey line with 50 in-line (red dots) and 2 off-line receivers (blue dots) that were deployed near Hanshui Park, Wuhan, China. The receiver spacing of the linear array numbered 1 to 50 is 2 m, and the receiver spacing between the two off-line receivers is 14 m. **b** A schematic diagram of the survey line (red line) and two off-line receivers (blue dots)
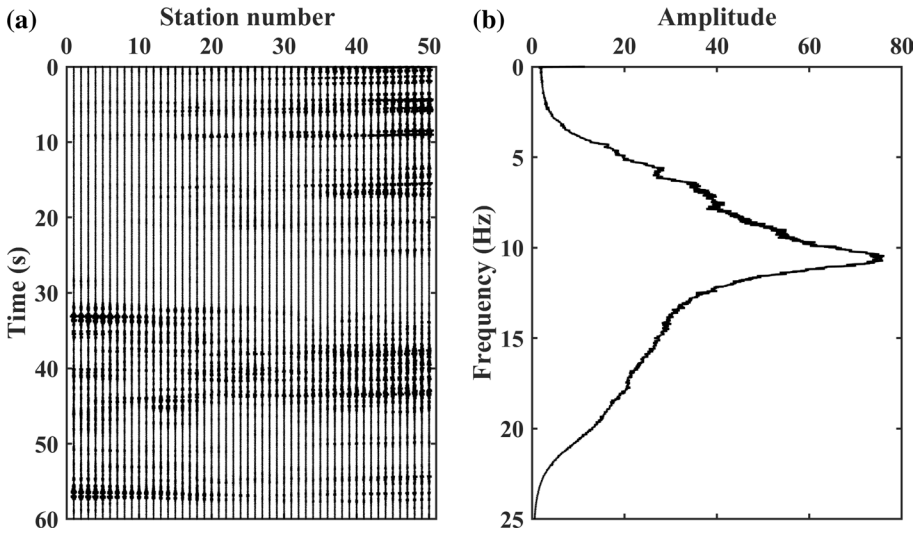
Fig. 16 **a** One 60-s segment of observed traffic-induced noise data (traces 1–50). **b** The average power spectrum of noise recordings generated from the traces 1–50
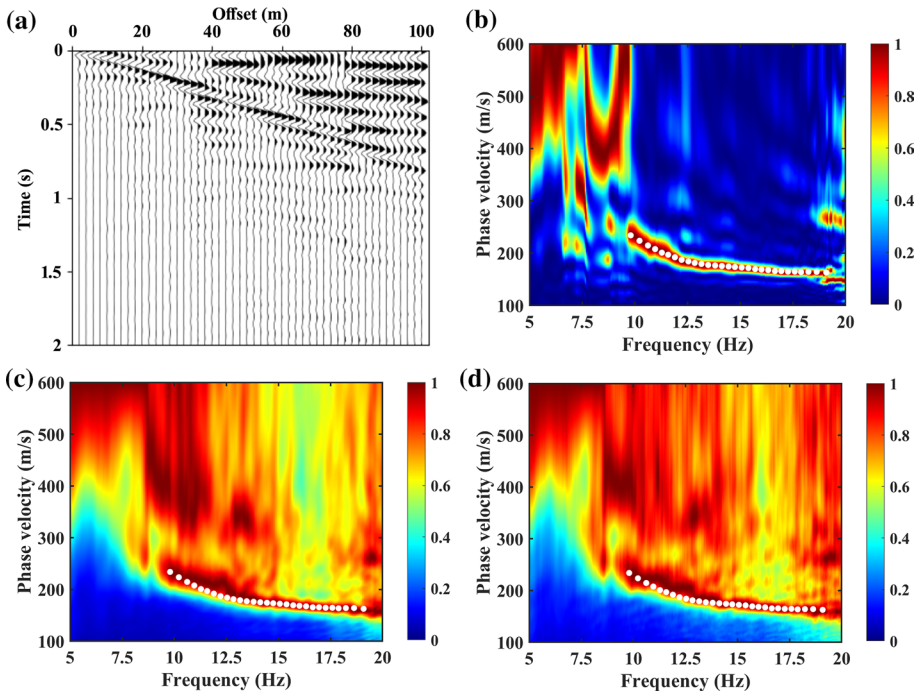

Fig. 17 **a** The virtual shot gather is generated from the full 4-h noise recording. **b** The dispersion image is calculated from the virtual shot gather shown in **a**. **c** The dispersion image is generated using the ReMi method. **d** The dispersion image is obtained using the roadside passive MASW method. The white dots in **b–d** denote the extracted dispersion curve by tracing the peak values of dispersion energy in **b**

roadside passive MASW methods (Fig. 17c, d) to produce dispersion images and put the dispersion curve in Fig. 17b on the dispersion images in Fig. 17c, d. The fundamental mode energy obtained by the SI method appears more continuous than that generated by the ReMi and roadside passive MASW methods. We plotted the hyperbolas for different frequencies (Fig. 18a) and obtained the first Fresnel angle (i.e., 11.8°) calculated from the wavelength at 19.1 Hz, to determine the azimuthal range of in-line noise sources. That is, the azimuthal range of in-line noise sources is from 157.5° to 181.1°, or from 337.5° to 1.1°. The Fresnel angle increases with the wavelength of plane waves (Fig. 18b). To estimate the accuracy of the dominant source azimuth, given a plane wave with a frequency of 15 Hz, a velocity of 300 m/s, and an azimuth of 60°, we calculated the ARF of real-world receivers' layout (Fig. 19b) and compared the result with that of the linear array (Fig. 19a). The result with many peaks (denoted by black crosses in Fig. 19c) indicates that the linear array based on beamforming is unable to reveal the correct noise source distribution. By incorporating data collected with the two offline receivers, the azimuth of noise sources was more accurately determined with the pseudo-linear array (Fig. 19d).

A unique peak (blue circle in Fig. 20a) can be searched in the beamforming output of each segment, which indicates the azimuth and phase velocity of noise sources. Figure 20b is generated from all segments and reveals the average azimuth of noise source distribution. This azimuth does not represent the dominant azimuth of other segments (Fig. 20c, d), instead it provides the average azimuthal effect of the noise source distribution over the recording time. Therefore, it is necessary to analyze the dominant azimuth of noise sources on each segment with ultrashort window length and apply our proposed scheme to select segments that positively contribute to the retrieval of surface waves. The range of surface-wave phase velocities is defined from 100 to 600 m/s based on the results in Fig. 17b–d. Under the constrained conditions including the azimuthal range of in-line noise sources and the desired range of surface-wave phase velocities, we picked useful segments to obtain the virtual shot gather and the dispersion image of surface waves. The results are generated using the selected segments in Fig. 21. By comparing Fig. 21a with Fig. 17a, some early arrivals before surface waves are effectively attenuated. The SNR (8.54) of the virtual shot gather (Fig. 21a) is greater than that (7.82) of the virtual shot gather in Fig. 17a. Furthermore, the dispersion image
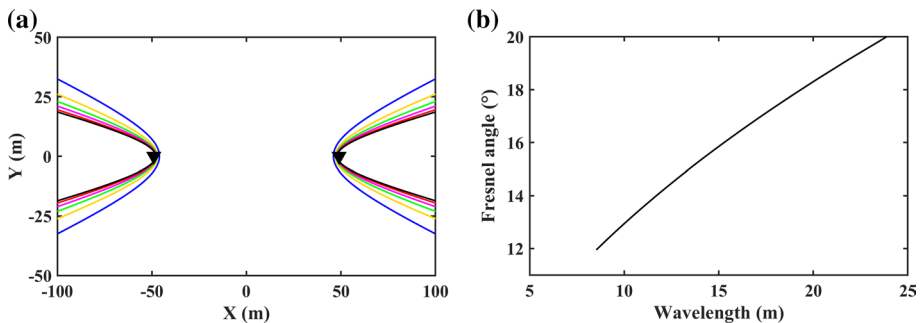
**Fig. 18** **a** The hyperbola for different frequencies 9.8 Hz (blue), 11.9 Hz (yellow), 13.8 Hz (green), 15.7 Hz (magenta), 17.6 Hz (red), and 19.1 Hz (black). The solid black triangles denote the receivers located at both ends of the array, in the 2D Cartesian coordinate system. The distance between these two receivers is 98 m. **b** The relationship between the Fresnel angles and the wavelengths
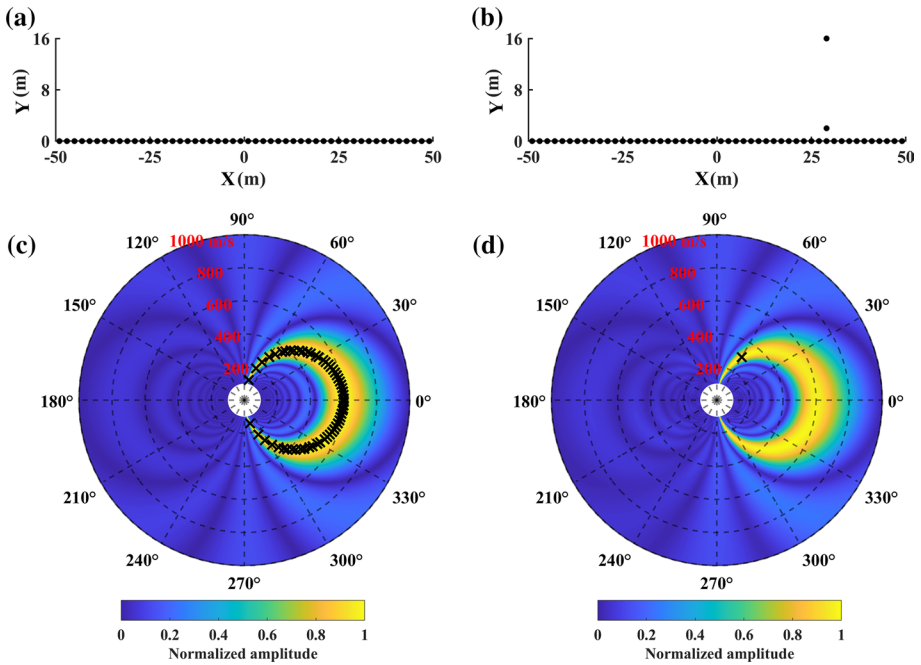
Fig. 19 The geometry of **a** a linear array and **b** a pseudo-linear array. Given a plane wave with a frequency of 15 Hz, a velocity of 300 m/s, and an azimuth of 60°, the ARFs of the linear and the pseudo-linear arrays shown in **c** and **d**, respectively. The black cross represents the peak value on the contour map
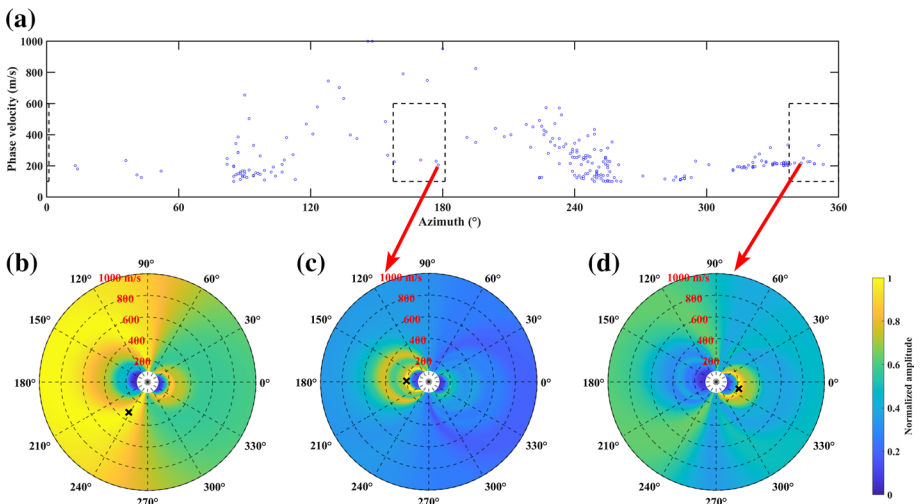
Fig. 20 **a** The values (blue circles) about the dominant azimuth of noise sources and the phase velocity obtained from the beamforming output of each segment. The black dashed boxes represent the constrained conditions. In the frequency band from 5 to 20 Hz, beamforming outputs from the **b** full noise data, **c** a 60-s segment affected by in-line noise sources located at the end of the survey line, and **d** another 60-s segment affected by in-line noise sources located at the head of the survey line. The black crosses as shown in **b**–**d** denote the peaks on the beamforming outputs, which are in the sources at 238°, 178°, and 343° azimuths, and the corresponding phase velocities of 328 m/s, 205 m/s, and 218 m/s, respectively
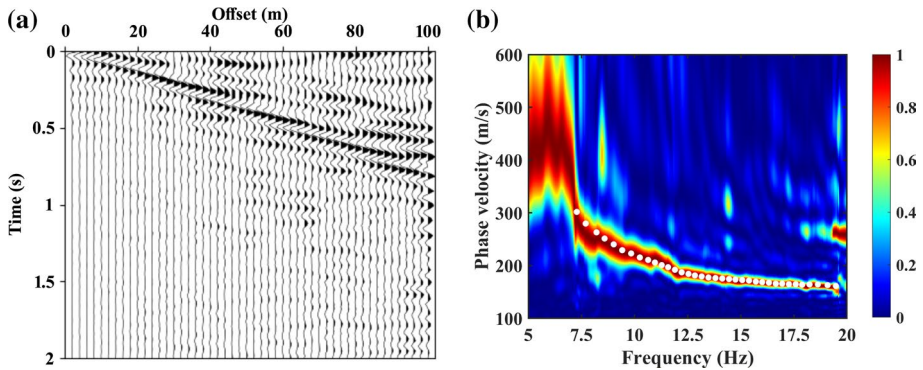
Fig. 21 **a** The virtual shot gather is generated from selected noise data. **b** The dispersion image is calculated from the virtual shot gather shown in **a**. The white dots represent the extracted dispersion curve of surface waves

(Fig. 21b) generated using the virtual shot gather from Fig. 21a extends to lower frequencies, from 9.8 to 7.3 Hz, compared to the virtual shot gather from Fig. 17a.

The inversion results (Fig. 22) generated from the dispersion curves in Fig. 17b and Fig. 21b are used to interpret the near-surface velocity structure. We considered the ranges of wavelengths from dispersion curves in Fig. 17b and Fig. 21b and designed two initial models 1 and 2 (Table 3), respectively. The measured dispersion curves generated from the all (Fig. 22a) and selected (Fig. 22b) segments match well with that calculated from the inverted models 1 and 2, respectively. Their corresponding RMS errors are reduced from 13.56 to 1.27 m/s and from 18.11 to 1.59 m/s after two iterations, respectively. The inversion result (Fig. 22c) indicates the dispersion curve with lower-frequency data from selected segments can penetrate greater depths than that from all segments, because the selected data possesses longer wavelengths that are more sensitive to the elastic properties of the deeper layers (Babuska and Cara 1991).

5 Discussion

Our selection scheme has the ability to pick useful segments in which the noise sources come from the stationary-phase zone defined by the Fresnel angle. It has also proven to be successful when optimally aligned noise sources are available in the recorded noise dataset. If dominant planar incoming surface waves propagate with an azimuth locating outside the stationary-phase zone, it may be a good choice to change the receiver array direction or deploy other linear arrays based on the dominant source azimuth (Guan et al. 2021; Morton et al. 2021). Meanwhile, we point out that a pseudo-linear array inherits the advantages of 1D and 2D arrays, which not only improve the accuracy of noise source location, but also reduce costs in field work.

In urban areas, the survey line is usually deployed along or parallel to the major roads. However, the distribution of noise sources changes with time due to complex human activities, so that it cannot be ensured that all noise sources always propagate along the survey line. As shown in Fig. 6a, the survey line is parallel to a major road. Figure 23a shows that the beamforming output with a dominant azimuth of 252° is
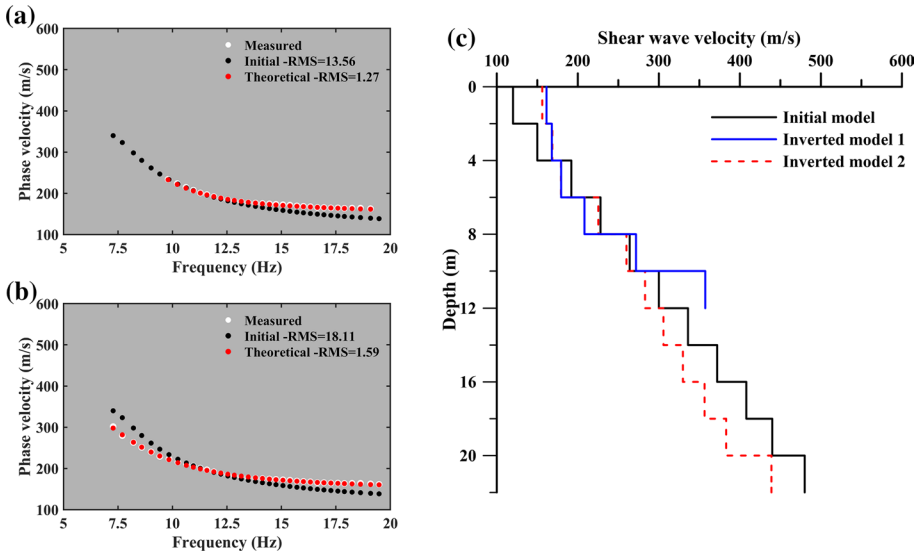
Fig. 22 a and **b** Comparison of the measured dispersion curves (white dots) obtained using the all and selected noise segments with the theoretical dispersion curves (red dots) calculated from the inverted models 1 and 2, respectively. The black dots denote the theoretical dispersion curve of the initial model 2 (Table 3). **c** Comparison of the inverted models 1 (solid blue line), 2 (dashed red line) with the S-wave velocities of the initial model (solid black line). The inverted model 1 was obtained by inversion of a fewer phase velocities (white dots in **a**) from all segments. The inverted model 2 was generated by inversion of more phase velocities (white dots in **b**) from selected segments

Table 3 Physical parameters of the initial models in the Wuhan example

Model		Layer number	V_S (m/s)	V_P (m/s)	ρ (kg/m³)	Thickness (m)
1	2	1	120	323	2000	2
		2	150	404	2000	2
		3	192	517	2000	2
		4	228	614	2000	2
		5	264	711	2000	2
		6	300	808	2000	2
		7	336	905	2000	2
		8	372	1000	2000	2
		9	408	1200	2000	2
		10	440	1400	2000	2
		11	480	1600	2000	Infinite

obtained from a removed segment that did not meet our constrained conditions. The dominant azimuth in a removed segment is located outside the stationary-phase zone. We also chose a selected segment to compare with the results in Fig. 23a–c. The results (Fig. 23e, f) generated using a selected segment are superior to those (Fig. 23b, c) using a removed segment. It indicates that the distribution of noise sources changes with time, especially in highly populated urban areas. It is unwise to use removed segments when stacking cross-correlations and dispersion images. This means that, applying the ReMi and roadside passive MASW methods on processing the noise data affect by off-line noise sources may not to produce high-quality dispersion images in urban environments, as illustrated by the results in Fig. 8b, c and Fig. 17c, d.

Although Park et al. (2004) and Le Feuvre et al. (2015) applied beamforming on multichannel noise records to obtain dispersion images, the phase velocities may be overestimated by off-line noise sources from some segments, and the dispersion images become blurred for stacking of poor images. Notice that using the scheme proposed by Le Feuvre et al. (2015) is unable to obtain unbiased phase velocities if unaligned noise sources are located too far from the 1D array. Meanwhile, we find that it can be difficult to lay out 2D arrays due to the accessibility of sites in residential areas. We adopted the strategy proposed by Liu et al. (2020) that adding two off-line receivers to form a pseudo-linear array can produce an unbiased dispersion image. It needs fewer receivers, fewer people, and much lower costs compared to the layout of the 2D arrays. Nevertheless, Liu et al. (2020) only focused on the processing of dispersion images. Our scheme can obtain the virtual shot gathers of surface waves with higher SNR, which is important for full waveform inversion and the estimation of seismic wave traveltime. The selection scheme shown in Zhou et al. (2018) is based on the asymmetry of the cross-correlation functions to highlight the symmetric parts of the segments of the functions that require randomly distributed or bidirectional noise sources. However, that case is rare in densely populated urban areas and the single directional noise sources are common. Our proposed scheme focuses on selecting in-line noise sources at one side of a survey line. The results shown previously indicate that our scheme possesses advantages in producing higher-SNR virtual shot gather, higher-resolution dispersion energy, and accurate S-wave velocities.
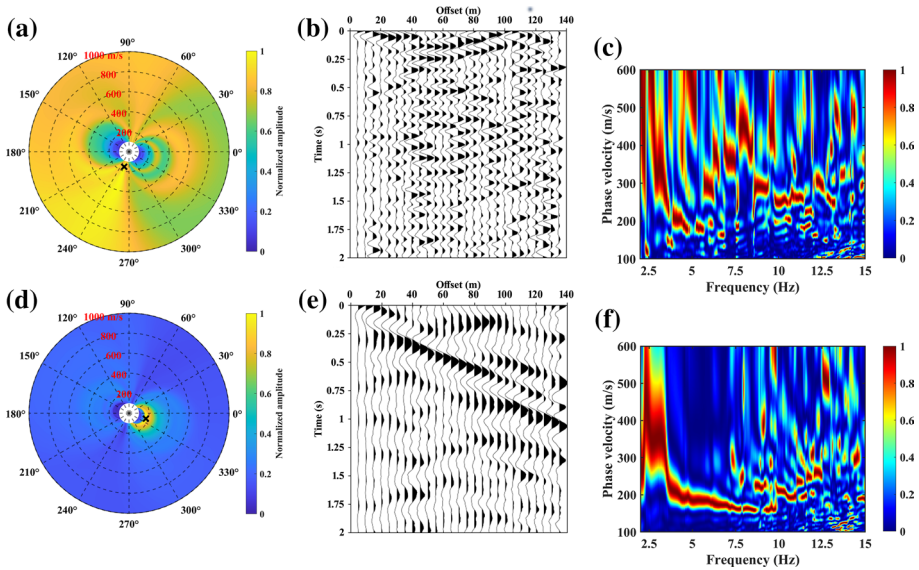
Fig. 23 Beamforming results, the virtual shot gathers, and dispersion images of surface waves generated from different segments acquired in Hangzhou experimental field. The results in **a**–**c** and **d**–**f** are generated using a removed segment and a selected segment, respectively. The black crosses as shown in **a**, **d** denote the peaks on the beamforming outputs, which are in the sources at 252° and 342° azimuths, and the corresponding phase velocities of 157 m/s and 176 m/s, respectively

6 Conclusions

This paper presents a beamforming-based segment selection scheme on processing traffic-induced noise, which is used for passive surface-wave surveys in densely populated urban environments. The proposed scheme has proven its validity by using beamforming on each segment to capture the spatial–temporal characteristics of noise source distribution. The advantage of analyzing the noise source distribution for each segment lies on avoiding the azimuthal effects from off-line noise sources and effectively picking out the segments affected by in-line noise sources. The noise segments are selected based on the given azimuthal range of in-line noise sources and a desired range of surface-wave phase velocity. The cross-correlation is performed on each selected stationary-phase segment, and the causal parts of cross-correlations are used for stacking to obtain the final virtual shot gather. The results show considerable improvements in SNR of the retrieved surface waves and obvious suppression on early arrivals compared to that using all segments. Using our scheme on processing traffic-induced noise, the SNR of a virtual shot gather is higher than the conventional method (i.e., SI) and the resolution of dispersion image is higher than that using SI, ReMi and roadside passive MASW methods. The inversion results demonstrate that our scheme can improve the estimation of S-wave velocities, due to the accessibility of more phase velocities. Our scheme can be regarded as an alternative tool for retrieving surface waves from traffic-induced noise, especially in urban environments with unevenly distributed of noise sources.

References

Afonin N, Kozlovskaya E, Nevalainen J, Narkilahti J (2019) Improving the quality of empirical Green's functions, obtained by crosscorrelation of high-frequency ambient seismic noise. Solid Earth 10:1621–1634

Aki K (1957) Space and time spectra of stationary stochastic waves, with spectral reference to microtremors. Bull Earthq Res Inst 35:415–456

Asten MW, Hayashi K (2018) Application of the spatial auto-correlation method for shear-wave velocity studies using ambient noise. Surv Geophys 39:633–659

Babuska V, Cara M (1991) Seismic anisotropy in the earth. Kluwer Academic Publishers, Boston, p 217

Bensen GD, Ritzwoller MH, Barmin MP, Levshin AL, Lin F, Moschetti MP, Shapiro NM, Yang Y (2007) Processing seismic ambient noise data to obtain reliable broad-band surface wave dispersion measurements. Geophys J Int 169:1239–1260

Cheng F, Xia J, Xu Y, Xu Z, Pan Y (2015) A new passive seismic method based on seismic interferometry and multichannel analysis of surface waves. J Appl Geophys 117:126–135

Cheng F, Xia J, Luo Y, Xu Z, Wang L, Shen C, Liu R, Pan Y, Mi B, Hu Y (2016) Multichannel analysis of passive surface waves based on crosscorrelations. Geophysics 81(5):EN57–EN66

Cheng F, Xia J, Xu Z, Hu Y, Mi B (2018) Frequency-wavenumber (FK)-based data selection in high-frequency passive surface wave survey. Surv Geophys 39(4):661–682

Cheng F, Xia J, Behm M, Hu Y, Pang J (2019) Automated data selection in the tau-p domain: application to passive surface wave imaging. Surv Geophys 40:1211–1228

Cheng F, Xia J, Zhang K, Zhou C, Ajo-Franklin JB (2021a) Phase-weighted slant stacking for surface wave dispersion measurement. Geophys J Int 226:256–269

Cheng F, Xia J, Ajo-Franklin JB, Behm M, Zhou C, Dai T, Xi C, Pang J, Zhou C (2021b) High-resolution ambient noise imaging of geothermal reservoir using 3C dense seismic nodal array and ultra-short observation. J Geophys Res Solid Earth 126:e2021JB021827

Curtis A, Gerstoft P, Sato H, Snieder R, Wapenaar K (2006) Seismic interferometry: turn noise into signal. Lead Edge 25:1082–1092

Dai T, Hu Y, Ning L, Cheng F, Pang J (2018) Effects due to aliasing on surface-wave extraction and suppression in frequency-velocity domain. J Appl Geophys 158:71–81

Dai T, Xia J, Ning L, Xi C, Liu Y, Xing H (2021) Deep leaning for extracting dispersion curves. Surv Geophys 42:69–95

Devi R, Sastry RG, Samadhiyan NK (2017) Assessment of soil-liquefaction potential based on geoelectrical imaging: a case study. Geophysics 82(6):B231–B243

Dorman J, Ewing M (1962) Numerical inversion of seismic surface wave dispersion data and crust-mantle structure in the New York-Pennsylvania area. J Geophys Res 67(13):5227–5241

Groos JC, Bussat S, Ritter JRR (2012) Performance of different processing schemes in seismic noise cross-correlations. Geophys J Int 188:498–512

Guan B, Mi B, Zhang H, Liu Y, Xi C, Zhou C (2021) Selection of noise sources and short-time passive surface wave imaging-a case study on fault investigation. J Appl Geophys 194:104437

Halliday D, Curtis A, Kragh E (2008) Seismic surface waves in a suburban environment: active and passive interferometric methods. Lead Edge 27(2):210–218

Humire F, Sáez E, Leyton F, Yañez G (2015) Combining active and passive multi-channel analysis of surface waves to improve reliability of $V_{S,30}$ estimation using standard equipment. Bull Earthq Eng 13:1303–1321

Ivanov J, Miller RD, Lacombe P, Johnson CD Jr, Lane JW (2006) Delineating a shallow fault zone and dipping bedrock strata using multichannel analysis of surface waves with a land streamer. Geophysics 71(5):A39–A42

Lawrence JF, Denolle M, Seats KJ, Prieto GA (2013) A numeric evaluation of attenuation from ambient noise correlation functions. J Geophys Res Solid Earth 118:6134–6145

Le Feuvre M, Joubert A, Leparoux D, Côte P (2015) Passive multi-channel analysis of surface waves with cross-correlations and beamforming. Application to a sea dike. J Appl Geophys 114:36–51

Lin CP, Chang CC, Chang TS (2004) The use of MASW method in the assessment of soil liquefaction potential. Soil Dyn Earthq Eng 24(9):689–698

Lin F, Moschetti MP, Ritzwoller MH (2008) Surface wave tomography of the western United States from ambient seismic noise: Rayleigh and Love wave phase velocity maps. Geophys J Int 173:281–298

Liu Y, Xia J, Cheng F, Xi C, Shen C, Zhou C (2020) Pseudo-linear-array analysis of passive surface waves based on beamforming. Geophys J Int 221:640–650

Liu Y, Xia J, Xi C, Dai T, Ning L (2021) Improving the retrieval of high-frequency surface waves from ambient noise through multichannel-coherency-weighted stack. Geophys J Int 227:776–785

Louie J (2001) Faster, better: Shear-wave velocity to 100 meters depth from refraction microtremor arrays. Bull Seismol Soc Am 91:347–364

Luo S, Luo Y, Zhu L, Xu Y (2016) On the reliability and limitations of the SPAC method with a directional wavefield. J Appl Geophys 126:172–182

Menon R, Gerstoft P, Hodgkiss WS (2012) Cross-correlations of diffuse noise in an ocean environment using eigenvalue based statistical inference. J Acoust Soc Am 132:3213–3224

Mi B, Xia J, Shen C, Wang L, Hu Y, Cheng F (2017) Horizontal resolution of multichannel analysis of surface waves. Geophysics 82(3):EN51–EN66

Mi B, Xia J, Bradford JH, Shen C (2020) Estimation near-surface shear-wave-velocity structures via multichannel analysis of Rayleigh and Love waves: an experiment at the Boise hydrogeophysical research site. Surv Geophys 41:323–341

Mi B, Xia J, Tian G, Shi Z, Xing H, Chang X, Xi C, Liu Y, Ning L, Dai T, Pang J, Chen X, Zhou C, Zhang H (2022) Near-surface imaging from traffic-induced surface waves with dense linear arrays: an application in the urban area of Hangzhou. China Geophys 87(2):B145–B158

Miller RD, Xia J, Park CB (1999) Multichannel analysis of surface waves to map bedrock. Lead Edge 18(12):1392–1396

Morton SL, Ivanov J, Peterie SL, Miller RD, Livers-Douglas AJ (2021) Passive multichannel analysis of surface waves using 1D and 2D receiver arrays. Geophysics 86(6):EN63–EN75

Nakata N (2016) Near-surface S-wave velocities estimated from traffic-induced Love waves using seismic interferometry with double beamforming. Interpretation 4(4):SQ23–SQ31

Ning L, Dai T, Liu Y, Xi C, Zhang H, Zhou C (2021) Application of multichannel analysis of passive surface waves method for fault investigation. J Appl Geophys 192:104382

Ning L, Xia J, Dai T (2022) High-frequency surface-wave imaging from traffic-induced noise by selecting inline sources. Mendeley Data. https://doi.org/10.17632/yv26tfc5x9.2

Pang J, Cheng F, Shen C, Dai T, Ning L, Zhang K (2019) Automatic passive data selection in time domain for imaging near-surface surface waves. J Appl Geophys 162:108–117

Park CB, Miller RD, Xia J (1998) Imaging dispersion curves of surface waves on multi-channel record. In: Society of Exploration and Geophysics (SEG), 68th Annual Meeting, New Orleans, Louisiana, pp 1377-1380

Park CB, Miller RD, Xia J (1999) Multichannel analysis of surface waves. Geophysics 64(3):800–808

Park CB, Miller RD, Xia J, Ivanov J (2004) Imaging dispersion curves of passive surface waves. 79th Annual International Meeting of the SEG, Expanded Abstracts. pp 1357–1360

Park C, Miller R (2008) Roadside passive multichannel analysis of surface waves (MASW). J Environ Eng Geophys 13:1–11

Prieto GA, Denolle M, Lawrence JF, Beroza GC (2011) On amplitude information carried by the ambient seismic field. Comptes Rendus Geosci 343:600–614

Rost S, Thomas C (2002) Array seismology: methods and applications. Rev Geophys 40(3):1008

Roux P, Sabra KG, Kuperman WA, Roux A (2005) Ambient noise cross correlation in free space: theoretical approach. J Acoust Soc Am 117(1):79–84

Roux P (2009) Passive seismic imaging with directive ambient noise: application to surface waves and the San Andreas Fault in Parkfield, CA. Geophys J Int 179:367–373

Sabra KG, Gerstoft P, Roux P, Kuperman WA, Fehler MC (2005) Extracting time-domain Greens function estimates from ambient seismic noise. Geophys Res Lett 32:L03310

Seats KL, Lawrence JF, Prieto GA (2012) Improved ambient noise correlation functions using Welch's method. Geophys J Int 188:513–523

Stehly L, Campillo M, Shapiro NM (2006) A study of the seismic noise from its long-range correlation properties. J Geophys Res 111:B10306

Sadeghisorkhani H, Gudmundsson O, Roberts R, Tryggvason A (2017) Velocity-measurement bias of the ambient noise method due to source directivity: a case study for the Swedish National Seismic Network. Geophys J Int 209:1648–1659

Schimmel M, Stutzmann E, Gallart J (2011) Using instantaneous phase coherence for signal extraction from ambient noise data at a local to a global scale. Geophys J Int 184(1):494–506

Seydoux L, de Rosny J, Shapiro NM (2017) Pre-processing ambient noise cross-correlations with equalizing the covariance matrix eigenspectrum. Geophys J Int 210:1432–1449

Shapiro NM, Campillo M (2004) Emergence of broadband Rayleigh waves from correlations of the ambient seismic noise. Geophys Res Lett 31:L07614

Snieder R (2004) Extracting the Green's function from the correlation of coda waves: a derivation based on stationary phase. Phys Rev E 69:046610

Song YY, Castagna JP, Black RA, Knapp RW (1989) Sensitivity of near-surface shear-wave velocity determination from Rayleigh and Love Waves. Expanded Abstracts of the 59th Annual Meeting of the Society of Exploration Geophysicists, Dallas, Texas, 509–512

Song Z, Zeng X, Xie J, Bao F, Zhang G (2021) Sensing shallow structure and traffic noise with fiber-optic internet cables in an urban area. Surv Geophys 42:1401–1423

Stephenson WJ, Louie JN, Pullammanappallil S, Williams RA, Odum JK (2005) Blind Shear-wave velocity comparison of ReMi and MASW results with boreholes to 200 m in Santa Clara Valley: implication for earthquake ground motion assessment. Bull Seismol Soc Am 95(6):2506–2516

Strobbia C, Cassiani G (2011) Refraction microtremors: data analysis and diagnostics of key hypotheses. Geophysics 76(3):MA11–MA20

Wapenaar K, Draganov D, Snieder R, Campman X, Verdel A (2010) Tutorial on seismic interferometry: part 1—Basic principles and applications. Geophysics 75(5):75A195-75A209

Weaver RL, Lobkis OI (2004) Diffuse fields in open systems and the emergence of the Green's function. J Acoust Soc Am 116(5):2731–2734

Wu CF, Huang HC (2019) Detection of a fracture zone using microtremor array measurement. Geophysics 84(1):B33–B40

Wu G, Dong H, Ke G, Song J (2020) An adapted eigenvalue-based filter for ocean ambient noise processing. Geophysics 85(1):KS29–KS38

Xi C, Xia J, Mi B, Dai T, Liu Y, Ning L (2021) Modified frequency-Bessel transform method for dispersion imaging of Rayleigh waves from ambient seismic noise. Geophys J Int 225:1271–1280

Xia J, Miller RD, Park CB (1999) Estimation of near-surface shear-wave velocity by inversion of Rayleigh waves. Geophysics 64(3):691–700

Xia J, Miller RD, Park CB, Ivanov J (2000) Construction of 2-D vertical shear-wave velocity field by the multichannel analysis of surface wave technique. Proceedings of the symposium on the application of geophysics to engineering and environmental problems (SAGEEP 2000), Arlington, VA, pp 1197–1206

Xia J, Miller RD, Park CB, Tian G (2003) Inversion of high frequency surface waves with fundamental and higher modes. J Appl Geophys 52(1):45–57

Xia J, Xu Y, Luo Y, Miller RD, Cakir R, Zeng C (2012) Advantages of using multichannel analysis of Love waves (MALW) to estimate near-surface shear-wave velocity. Surv Geophys 33:841–860

Xie J, Yang Y, Luo Y (2020) Improving cross-correlations of ambient noise using an rms-ratio selection stacking method. Geophys J Int 222:989–1002

Xu Y, Lebedev S, Meier T, Bonadio R, Bean CJ (2021) Optimized workflows for high-frequency seismic interferometry using dense arrays. Geophys J Int 227(2):875–897

Xu Z, Mikesell TD (2017) On the reliability of direct Rayleigh-wave estimation from multicomponent cross-correlations. Geophys J Int 210:1388–1393

Xu Z, Mikesell TD, Xia J, Cheng F (2017) A comprehensive comparison between the refraction microtremor and seismic interferometry methods for phase-velocity estimation. Geophysics 82(6):EN99–EN108

Yilmaz Ö, Eser M, Berilgen M (2006) A case study of seismic zonation in municipal areas. Lead Edge 25(3):319–330

Zhang Y, Li YE, Zhang H, Ku T (2019) Near-surface site investigation by seismic interferometry using urban traffic noise in Singapore. Geophysics 84(2):B169–B180

Zhou C, Xi C, Pang J, Liu Y (2018) Ambient noise data selection based on the asymmetry of cross-correlation functions for near surface applications. J Appl Geophys 159:803–813

Zhou C, Xia J, Pang J, Cheng F, Chen X, Xi C, Zhang H, Liu Y, Ning L, Dai T, Mi B, Zhou C (2021) Near-surface geothermal reservoir imaging based on the customized dense seismic network. Surv Geophys 42:673–697

Zhou C, Xia J, Cheng F, Pang J, Chen X, Xing H, Chang X (2022) Passive surface-wave waveform inversion for source-velocity joint imaging. Surv Geophys. https://doi.org/10.1007/s10712-022-09691-7

Publisher's Note Springer Nature remains neutral with regard to jurisdictional claims in published maps and institutional affiliations.